

# New Constraints on Dark Photon Dark Matter with a Millimeter-Wave Dielectric Haloscope

Guoqing Wei,<sup>1,2,3</sup> Diguang Wu,<sup>1,2,3</sup> Runqi Kang,<sup>1,2,3</sup> Qingning  
Jiang,<sup>1,2</sup> Man Jiao,<sup>4,5,6,\*</sup> Xing Rong,<sup>1,2,3,†</sup> and Jiangfeng Du<sup>1,2,3,4,5</sup>

<sup>1</sup>*CAS Key Laboratory of Microscale Magnetic Resonance and School of Physical Sciences,  
University of Science and Technology of China, Hefei 230026, China*

<sup>2</sup>*Anhui Province Key Laboratory of Scientific Instrument Development and Application,  
University of Science and Technology of China, Hefei 230026, China*

<sup>3</sup>*Hefei National Laboratory, University of Science and Technology of China, Hefei 230088, China*

<sup>4</sup>*Institute for Advanced Study in Physics, Zhejiang University, Hangzhou 310027, China*

<sup>5</sup>*Institute of Quantum Sensing and School of Physics, Zhejiang University, Hangzhou 310027, China*

<sup>6</sup>*Zhejiang Key Laboratory of R&D and Application of Cutting-edge  
Scientific Instruments, Zhejiang University, Hangzhou, 310027, China*

Dark matter remains one of the most profound and unresolved mysteries in modern physics. To unravel its nature, numerous haloscope experiments have been implemented across various mass range. However, very few haloscope experiments conducted within millimeter-wave frequency range, which is in the favored mass region for well-motivated dark matter candidates. Here we designed and constructed a millimeter-wave dielectric haloscope featuring a dark matter detector composed of dielectric disks and a mirror. Using this setup, we conducted a search for dark photon dark matter and found no evidence for its existence. Our results established new constraints on the kinetic mixing parameter in the mass range from 387.72 to 391.03  $\mu\text{eV}$ , improving the existing limits by two orders of magnitude. With future enhancements, our system has the potential to explore new parameter space for dark photon as well as axion dark matter within millimeter-wave frequency range.

An abundance of astrophysical observation results [1–6] indicate that the majority of the mass of universe exists in some unknown form, which is called dark matter [7–9]. Although the nature of dark matter remains elusive, numerous hypotheses have been proposed to explain its composition. Among these, dark photon, a hypothetical spin-1 gauge boson, has garnered significant attention in recent years [10–12]. As a ultralight dark matter candidate, dark photon is theoretically well-motivated and possesses varied production mechanisms [13–17]. Dark photon is characterized by the kinetic mixing with the ordinary photon as follows [18, 19]:

$$\mathcal{L} = -\frac{1}{4}F_{\mu\nu}^2 - \frac{1}{4}V_{\mu\nu}^2 - \frac{1}{2}m_{A'}^2 A'_\mu A'^\mu + \frac{1}{2}\chi F_{\mu\nu} V^{\mu\nu}, \quad (1)$$

where  $A_\mu$  and  $A'_\mu$  denote the fields of ordinary photon and dark photon, respectively,  $F_{\mu\nu} = \partial_\mu A_\nu - \partial_\nu A_\mu$  and  $V_{\mu\nu} = \partial_\mu A'_\nu - \partial_\nu A'_\mu$  are the corresponding field tensors. Kinetic mixing  $\chi$  and dark photon mass  $m_{A'}$  construct the parameter space of dark photon. This kind of interaction will modify the Maxwell equations by introducing a “dark” current density  $\mathbf{J}_{\text{DM}}$  as [20, 21]

$$\mathbf{J}_{\text{DM}} = \chi\epsilon_0 \left( \frac{\partial \mathbf{E}_{\text{DM}}}{\partial t} - c^2 \nabla \times \mathbf{B}_{\text{DM}} \right), \quad (2)$$

where  $\mathbf{E}_{\text{DM}} = \partial_t \mathbf{A}'$  and  $\mathbf{B}_{\text{DM}} = \nabla \times \mathbf{A}'$  are dark photon electric and magnetic field, respectively,  $\epsilon_0$  is the vacuum permittivity and  $c$  is the speed of light. The “dark” current density oscillates at the frequency of  $f_{\text{DM}} = m_{A'} c^2 / h$ , which is determined by dark photon

mass  $m_{A'}$ . This “dark” current density will induce photons with the same frequency of  $f_{\text{DM}}$  within the probe, such as a cavity which is the most widely used in haloscope experiments. Dark photon dark matter could be produced by quantum fluctuations during inflation [13]. In this mechanism, well-motivated dark photon mass as  $m_{A'} \gtrsim 10^{-5}$  eV (i.e.,  $f_{\text{DM}} \gtrsim 2$  GHz) is yielded from the cosmological constraints on Hubble scale [22]. Many experiments have been implemented to search for dark photons at different mass ranges [23–28], yet the millimeter-wave frequency range remains rarely explored. It is challenging to conduct haloscope experiment with cavity at such high frequency, due to the deterioration of quality factor and decrease of effective mode volume with increasing frequency. Many alternative methods aiming high frequency range have been proposed, such as dish antenna [26], metal plate [29], dielectric stack [30] and quantum cyclotron [24]. The dielectric stack is a promising haloscope due to the wide search band and high dark-photon-to-photon conversion rate. Recently, dielectric stack has been utilized to search for dark photons at centimeter-wave [28] and optical frequency range [23, 31], while the millimeter-wave frequency range remains untouched.

In this paper, we designed and implemented a dielectric haloscope within the millimeter-wave frequency range. To convert dark photons to photons with high efficiency, we constructed a millimeter-wave stack consisting of four dielectric disks and a mirror. An antenna together with a millimeter-wave receiver chain were implemented to detect the dark photon signal with

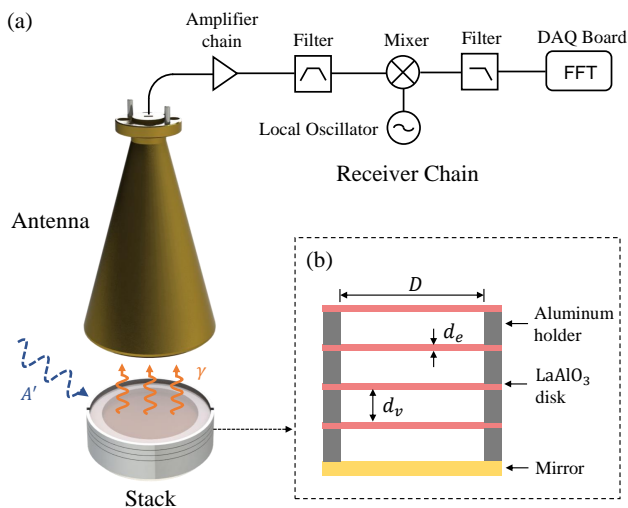


FIG. 1. Experimental Setup. (a) Simplified diagram of the experiment apparatus for dark photon search.  $A'$  and  $\gamma$  stand for the dark photon field and the converted photons, respectively. The emitted photons  $\gamma$  are gathered by an antenna, which has a aperture of 39.2mm. The receiver chain is to detect the gathered signal with high efficiency. (b) Diagram of dielectric stack. The stack is comprised of one gold-coating aluminum mirror and four LaAlO<sub>3</sub> disks with refractive index  $n \approx 5$ . The disks and mirror are separated by aluminum holders. The inner diameter of the holder is  $D \approx 32.0$ mm, while  $d_v \approx 1.580$ mm and  $d_e \approx 0.320$ mm denote the spacing and thickness of the disks, respectively.

low noise. Additionally, to enhance the dark photon search efficiency we employed the data acquisition (DAQ) board based on field programmable gate array (FPGA) to achieve a 100% duty cycle. With total acquisition time of eight days, our prototype established new constraints on kinetic mixing  $\chi$  in the mass range from 387.72 to 391.03  $\mu\text{eV}$ , corresponding to the frequency from 93.750 to 94.550 GHz.

Our haloscope apparatus consisted of three parts: dielectric stack, antenna and receiver chain, as shown in Fig. 1(a). The dielectric stack was the fundamental component where dark photons were converted to photons. As shown in Fig. 1(b), four parallel dielectric disks and a mirror were meticulously arranged with particular spacing  $d_v$ , which was determined by the aluminum holders. Under the driving of “dark” current density  $\mathbf{J}_{\text{DM}}$ , photons were emitted at each interface of the dielectric material and air due to the different refractive indices [32]. We chose the half-wave stack, which meant photons with corresponding frequency  $f_0$  would accumulate  $\pi$  phase passing through each disk or air gap. Thus, the photons converted at every interface would be superposed coherently, and the conversion rate increased as the square of dielectric disk number  $N$ . We positioned a gold-coating mirror on one side of the dielectric stack to reflect photons emitted in that

direction, and achieved a fourfold increase in the overall conversion rate on the opposite side. In this dielectric stack, the power of the emitted photons can be expressed as [26, 33]

$$P = \chi^2 c \rho_{\text{DM}} A \langle \cos^2 \theta \rangle |\mathcal{B}|^2, \quad (3)$$

where  $\rho_{\text{DM}}$  is the local density of dark photon dark matter, in this paper  $\rho_{\text{DM}}$  is set as 0.45 GeV/cm<sup>3</sup> [34],  $A$  is the area of dielectric disk, and  $\theta$  denotes the angle between the polarization of dark photon and experimental receiver system. We assume the dark photon is random polarized, and  $\langle \cos^2 \theta \rangle$  equals 1/3 [35].  $|\mathcal{B}|^2$  is the amplification parameter of stack conversion rate due to the constructive interference, which is dependent on the frequency of dark photons. For a perfect half-wave dielectric stack,  $|\mathcal{B}|^2 = 4N^2(1 - 1/n^2)^2$  when dark photons occur at the center frequency  $f_0$  of stack, where  $n$  is the refractive index of dielectric disks.

The material of the disks was chosen to be LaAlO<sub>3</sub>, with refractive index  $n \approx 5$ . To construct a half-wave stack with center frequency around 94 GHz, the thickness  $d_e$  and spacing  $d_v$  of the disks were carefully designed as 0.320 mm and 1.580 mm, respectively. The low dielectric loss angle  $\delta_e$  of LaAlO<sub>3</sub> [36] would benefit the dark photon conversion rate, by minimizing the energy loss of induced photons while passing through the disks. The surfaces of dielectric disks and mirror were carefully polished. The gold coating of mirror was designed as 2  $\mu\text{m}$ , which was much larger than the skin depth in gold ( $\sim 250$  nm). Notably, this half-wave stack exhibited robust against the imperfections in disk thickness and spacing due to the machining and installation error.

A linear polarized antenna was positioned above dielectric stack to gather the dark photon-converted photons. In the frequency range we concerned, the receiving efficiency of the antenna was around 0.48 (see more details in Appendix C). During the dark photon search experiment, the antenna polarization remained in the latitudinal direction, and it was sensitive to dark photons with the same polarization direction. The antenna and stack were placed in a metal shielding to isolate the environmental electromagnetic noise. After being coupled into waveguide by antenna, the dark photon signal entered the receiver chain to be detected. The millimeter-wave low noise amplifier chain in receiver chain amplified the dark photon signal by a total gain of  $\sim 60$  dB. The signal was then down-converted to baseband frequency below 205 MHz through multi-stage filtering and mixing. A millimeter-wave local oscillator supplied a local oscillating signal with a tunable frequency from 93.7 GHz to 94.4 GHz. To analyse the frequency domain properties of the signal, we employed a DAQ board (JYTEK, JY-9824) acting as a real-time spectrum analyzer with bandwidth of 250 MHz. To improve the dark photon search efficiency, the DAQ

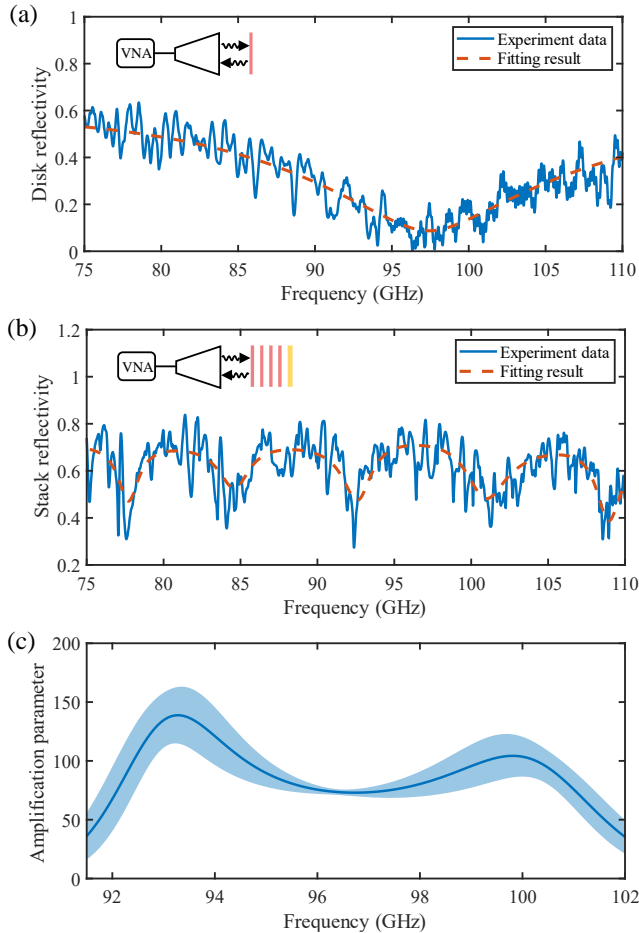


FIG. 2. Results of amplification parameter calibration with the reflectivity test method. (a) The reflectivity of the first dielectric disk (the bottom one in the stack). The blue solid line is the measurement data, and the red dashed line is the fitting result with  $\mathcal{R}$ . The inset shows the scheme of reflectivity test using the vector network analyzer (VNA). (b) The reflectivity of stack. The blue solid line and red dashed line stand for experiment data and the fitting result with the one-dimension multiple layers model, respectively. (c) Amplification parameter as a function of frequency. This blue solid line denotes the characterized result of stack amplification parameter. The shaded region denotes  $\pm 1\sigma$  interval.

board was updated to enable parallel data acquisition and Fourier transformation with no dead time.

The expected dark photon signal is proportional to the amplification parameter  $|\mathcal{B}|^2$ , which should be carefully characterized. The amplification parameter  $|\mathcal{B}|^2$  is determined by the thicknesses  $d_e$ , spacing  $d_v$ , refractive indices  $n$  and loss angles  $\delta$  of the LaAlO<sub>3</sub> disks [32]. The loss angle  $\delta$  includes two parts. One is the dielectric loss  $\delta_e$  of LaAlO<sub>3</sub> material. The other is the extra loss caused by some three-dimension effects like the tilts of disks in the stack, which is modeled as effective loss angle  $\delta_{\text{eff}}$ . Thus, the loss angles  $\delta$  will vary with different disk

installation. To characterize the amplification parameter of the stack employed in this work, the parameters above were accurately calibrated by carefully designed procedures. The thicknesses  $d_e$  of the four LaAlO<sub>3</sub> disks were  $0.312 \pm 0.007$  mm,  $0.311 \pm 0.007$  mm,  $0.308 \pm 0.006$  mm and  $0.319 \pm 0.006$  mm (from bottom to top in Fig. 1(b)), which were obtained by a spiral micrometer. The rest stack parameters were calibrated by reflectivity test with a millimeter-wave vector network analyzer (Ceyear, 3672C). Firstly, the reflectivity test of every LaAlO<sub>3</sub> disk was implemented. The reflectivity of a single dielectric disk can be represented as [32]

$$\mathcal{R} = \eta \left| \frac{(\tilde{n}^2 - 1) \sin \Delta}{2i\tilde{n} \cos \Delta + (\tilde{n}^2 + 1) \sin \Delta} \right|, \quad (4)$$

where  $\eta < 1$  results from the energy loss while antenna emitting and receiving the photons.  $\Delta = \tilde{n}\omega d_e/c$  denotes the phase change of photons when going through the disk, where  $\omega$  is the frequency, and  $\tilde{n} = ne^{i\delta_{\text{single}}/2}$  is the complex refractive index including the loss angle  $\delta_{\text{single}}$  within the single disk test. The reflectivity of the first LaAlO<sub>3</sub> disk (the bottom one in Fig. 1(b)) is shown in Fig. 2(a). By fitting the experiment result with  $\mathcal{R}$ , the refractive index  $n$  was extracted as  $4.93 \pm 0.11$ . Reflectivity test of the other LaAlO<sub>3</sub> disks resulted in  $n$  as  $4.89 \pm 0.11$ ,  $4.94 \pm 0.10$  and  $4.91 \pm 0.09$ , respectively (see more details in Appendix B). Then the stack reflectivity test was implemented to obtain loss angles  $\delta$  and spacing  $d_v$ . The result is shown in Fig. 2(b). By fitting experiment data to the one-dimension multiple layers model [32], the spacing  $d_v$  were given as  $1.545 \pm 0.021$  mm,  $1.569 \pm 0.015$  mm,  $1.570 \pm 0.022$  mm, and  $1.560 \pm 0.008$  mm, respectively. The loss angles  $\delta$  were also obtained as  $(9.89 \pm 2.57) \times 10^{-3}$ ,  $(5.30 \pm 2.94) \times 10^{-3}$ ,  $(1.14 \pm 0.32) \times 10^{-2}$  and  $(1.17 \pm 0.29) \times 10^{-2}$ , respectively. Due to the extra loss caused by three-dimension effects, the loss angles  $\delta$  were larger than the LaAlO<sub>3</sub> dielectric loss angle  $\delta_e$ , which is  $\sim 3 \times 10^{-3}$  at room temperature[37].

The characterized amplification parameter  $|\mathcal{B}|^2$  is shown in Fig. 2(c), which was obtained from the one-dimension multiple layers model. The sensitive range of our stack was from 92 GHz to 101 GHz, covering a broad frequency bandwidth of around 9 GHz. The most sensitive frequency was nearby 93.3 GHz, where the amplification parameter  $|\mathcal{B}|^2$  achieved 139. From 93.750 GHz to 94.550 GHz, the amplification parameter varied from 102 to 130. The relative uncertainty was around  $\mathcal{O}(10^{-1})$ , which was given by the Monte Carlo method involving the uncertainties of stack parameters.

The data acquisition procedures were conducted within the period from 2025-01-13 to 2025-01-22. We conducted the data acquisition at eight overlapped frequency ranges, covering a overall range from 93.750 to 94.550 GHz (see more details in Appendix E). At each frequency range, the data acquisition time  $t_{\text{tot}}$  was about

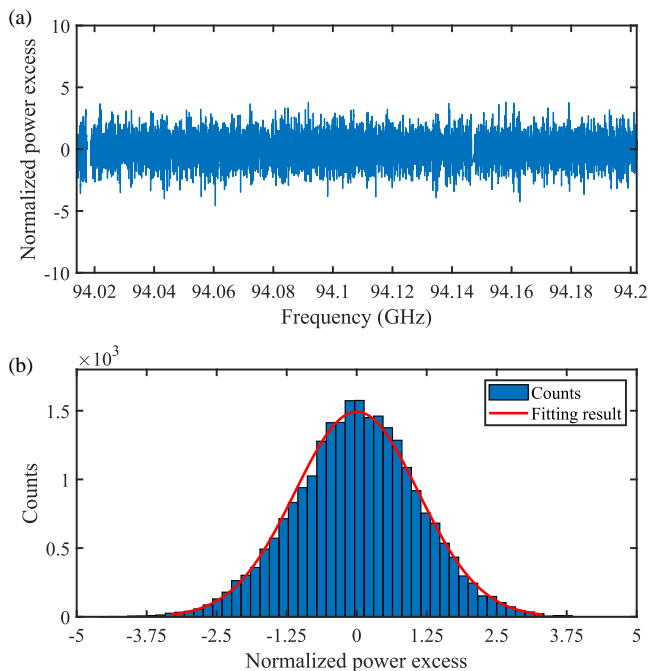


FIG. 3. Data analysis of the frequency range from 94.014 GHz to 94.202 GHz. (a) The normalized power excess after convolution. The bins around each spurious signal are already discarded. (b) The normalized power excess distribution. The blue bars are the counts of every power excess value range and the red solid line is the fitting result with normal Gaussian distribution.

24 hours and a total number of  $N_{\text{tot}} \approx 5 \times 10^8$  spectra were acquired. The frequency bin width  $\delta f$  of each spectrum was set as 7.63 kHz. The spectra were first averaged on the DAQ hardware of  $5.1 \times 10^3$  times and then saved, resulting in around  $1 \times 10^5$  spectra.

The data analysis procedures of the eight frequency ranges were the same and here we take the frequency range from 94.014 GHz to 94.202 GHz as an example. The saved spectra number was 124010, and they were averaged to a single raw spectrum. Firstly, the raw power spectrum was filtered with a 4th-order Savitzky-Golay (SG) filter with a window length of 1.14 MHz [38]. By dividing the spectrum baseline obtained from the SG filter, the raw power spectrum was transformed to raw power excess. In the raw power excess, there was a candidate peak sticking out at 94.147 GHz. Since it was not found in the result of neighboring frequency range, this peak was identified as a spurious signal and ruled out. In the following analysis procedures, bins that occupied by the spurious signals were discarded (see more details in Appendix E). The baseline removal operation would attenuate a potential dark photon signal by  $\eta_{\text{SG}} = 0.74$  which was obtained from analysis on a simulated dark photon signal. Since the expected dark photon signal would occupy tens of bins, the raw power excess was convolved with the dark photon line shape to enhance

SNR [38]. Then the convolved power excess was divided by its standard deviation to obtain the normalized power excess, as shown in Fig. 3(a). There were no bins exceeding  $5\sigma$  in the normalized power excess, and it satisfied the normal Gaussian distribution  $N(\mu, \sigma^2)$ . The parameters of mean  $\mu = -0.0004 \pm 0.0131$  and standard deviation  $\sigma = 1.1035 \pm 0.0097$  were obtained from fitting result, as illustrated by the red line in Fig. 3(b). The mean value  $\mu$  was slightly larger than one due to the correlations induced by convolution.

Our result gives non observation of any possible dark photon signal within our detection bandwidth, since the candidate peaks are all ruled out through analysis (see more details in Appendix E). Based on that, the 90% confidence constraints on kinetic mixing  $\chi$  are given by Bayesian analysis, which is developed in ADMX experiment [38]. The results of eight frequency ranges are combined by selecting the lower constraints at overlapped bins, as shown in Fig. 4(a). We establish the most stringent constraints that  $\chi < 2.0 \times 10^{-11}$  in the dark photon mass region from 387.72  $\mu\text{eV}$  to 391.03  $\mu\text{eV}$ , except the total 420 bins around four spurious signals. An upper limit of  $\chi < 5.78 \times 10^{-12}$  is achieved at 387.73  $\mu\text{eV}$ , which improves the existing limits [39] by more than 120 times. Constraints from other haloscope searches in extended mass range are shown in Fig. 4(b). This work sets the most stringent constraints within W band.

In summary, we constructed a millimeter-wave dielectric stack haloscope with four LaAlO<sub>3</sub> disks. Based on this dielectric haloscope, we launched the wide-band search for dark photon dark matter. In the range of dark photon masses from 387.72  $\mu\text{eV}$  to 391.03  $\mu\text{eV}$ , we achieved the most stringent constraints on kinetic mixing, which improves the existing limits by two orders of magnitude. In the future, by introducing cryogenic amplifiers with lower noise, such as SIS mixer, the constraints could be further improved by a factor of  $\sim 3$ . By enhancing the millimeter-wave local oscillator, we could explore a wider dark photon mass range of 380.48  $\sim$  417.70  $\mu\text{eV}$  with the same stack. Furthermore, our dielectric haloscope could also search for axion dark matter, if the stack is placed in a steady magnetic field which is parallel to the dielectric disks. By utilizing the narrow-band but more sensitive stack mode and increasing disk number, we may give new constraints on axion-photon coupling parameter within millimeter-wave frequency range.

This work was supported by NSFC (T2388102, 12205290, 12261160569), the Innovation Program for Quantum Science and Technology (2021ZD0302200), and the National Key R&D Program of China (Grant No. 2021YFC2203100). X.R. thanks the support by the Major Frontier Research Project of the University of Science and Technology of China (Grant No. LS9990000002). M.J. thanks the Fundamental Research

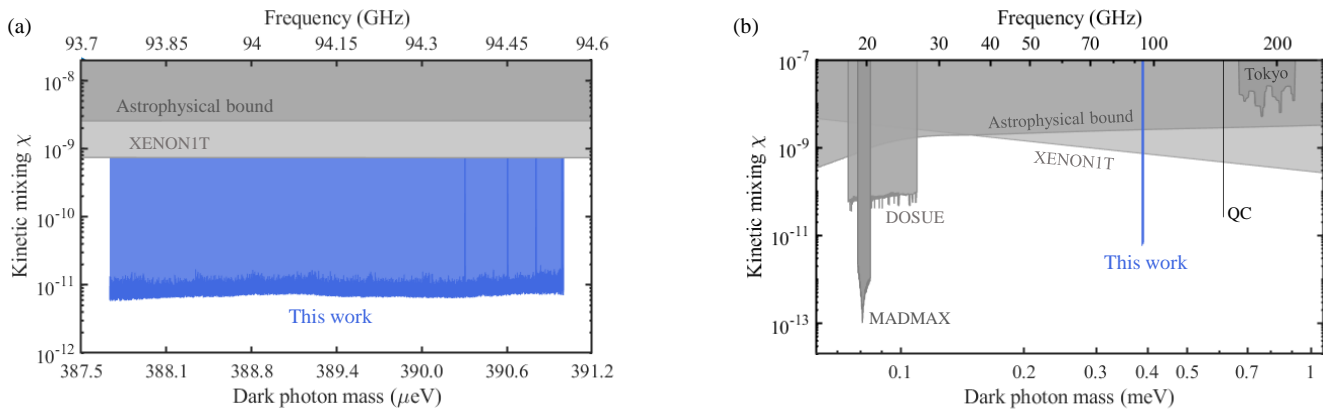


FIG. 4. Constraints on the dark photon with kinetic mixing  $\chi$  and dark photon mass. (a) The blue shaded region shows the 90% confidence limits set by this work. The light gray region refers to the result of XENONIT [39], and the deep gray region is the astrophysical bound set by Arias et al [40]. (b) This work along with other experimental searches in extended dark photon mass range. Constraints on kinetic mixing from MADMAX [28], DOSUE [29], QC [24] and Tokyo [41] are shown in gray.

Funds for Central Universities.

\* man.jiao@zju.edu.cn

† xrong@ustc.edu.cn

- [1] V. C. Rubin and W. K. Ford, Jr., *The Astrophysical Journal* **159**, 379 (1970).
- [2] V. C. Rubin, W. K. Ford, Jr., N. Thonnard, and D. Burstein, *The Astrophysical Journal* **261**, 439 (1982).
- [3] K. G. Begeman, A. H. Broeils, and R. H. Sanders, *Monthly Notices of the Royal Astronomical Society* **249**, 523 (1991).
- [4] J. A. Tyson, G. P. Kochanski, and I. P. Dell’Antonio, *The Astrophysical Journal* **498**, L107 (1998).
- [5] A. N. Taylor, S. Dye, T. J. Broadhurst, N. Benitez, and E. v. Kampen, *ApJ* **501**, 539 (1998).
- [6] D. Clowe, M. Bradac, A. H. Gonzalez, M. Markevitch, S. W. Randall, C. Jones, and D. Zaritsky, *ApJ* **648**, L109 (2006).
- [7] V. Trimble, *Annual Review of Astronomy and Astrophysics* **25**, 425 (1987).
- [8] J. L. Feng, *Annu. Rev. Astron. Astrophys.* **48**, 495 (2010).
- [9] G. Bertone and D. Hooper, *Rev. Mod. Phys.* **90**, 045002 (2018).
- [10] M. Battaglieri *et al.*, [arXiv:1707.04591](https://arxiv.org/abs/1707.04591).
- [11] J. Billard, M. Boulay, S. Cebrián, L. Covi, G. Fiorillo, A. Green, J. Kopp, B. Majorovits, K. Palladino, F. Petricca, *et al.*, *Rep. Prog. Phys.* **85**, 056201 (2022).
- [12] A. Caputo, A. J. Millar, C. A. J. O’Hare, and E. Vitagliano, *Phys. Rev. D* **104**, 095029 (2021).
- [13] P. W. Graham, J. Mardon, and S. Rajendran, *Phys. Rev. D* **93**, 103520 (2016).
- [14] J. A. Dror, K. Harigaya, and V. Narayan, *Phys. Rev. D* **99**, 035036 (2019).
- [15] P. Agrawal, N. Kitajima, M. Reece, T. Sekiguchi, and F. Takahashi, *Physics Letters B* **801**, 135136 (2020).
- [16] A. Ahmed, B. Grzadkowski, and A. Socha, *J. High Energ. Phys.* **2020** (8), 59.
- [17] R. T. Co, A. Pierce, Z. Zhang, and Y. Zhao, *Phys. Rev. D* **99**, 075002 (2019).
- [18] B. Holdom, *Physics Letters B* **178**, 65 (1986).
- [19] B. Holdom, *Physics Letters B* **166**, 196 (1986).
- [20] F. P. Huang and H.-S. Lee, *Int. J. Mod. Phys. A* **34**, 1950012 (2019).
- [21] G. Marocco, [arXiv:2110.02875](https://arxiv.org/abs/2110.02875).
- [22] Y. Akrami and et al., *A&A* **641**, A10 (2020).
- [23] J. Chiles, I. Charaev, R. Lasenby, M. Baryakhtar, J. Huang, A. Roshko, G. Burton, M. Colangelo, K. Van Tilburg, A. Arvanitaki, *et al.*, *Phys. Rev. Lett.* **128**, 231802 (2022).
- [24] X. Fan, G. Gabrielse, P. W. Graham, R. Harnik, T. G. Myers, H. Ramani, B. A. Sukra, S. S. Wong, and Y. Xiao, *Phys. Rev. Lett.* **129**, 261801 (2022).
- [25] H. An, S. Ge, W. Q. Guo, X. Huang, J. Liu, and Z. Lu, *Phys. Rev. Lett.* **130**, 181001 (2023).
- [26] S. Knirck, *et al.*, and BREAD Collaboration, *Phys. Rev. Lett.* **132**, 131004 (2024).
- [27] R. Kang, M. Jiao, Y. Tong, Y. Liu, Y. Zhong, Y.-F. Cai, J. Zhou, X. Rong, and J. Du, *Phys. Rev. D* **109**, 095037 (2024).
- [28] J. Egge *et al.* (MADMAX Collaboration), [arXiv:2408.02368](https://arxiv.org/abs/2408.02368).
- [29] S. Kotaka *et al.* (DOSUE-RR Collaboration), *Phys. Rev. Lett.* **130**, 071805 (2023).
- [30] A. Caldwell *et al.* (MADMAX Collaboration), *Phys. Rev. Lett.* **118**, 091801 (2017).
- [31] L. Manenti, U. Mishra, G. Bruno, H. Roberts, P. Oikonomou, R. Pasricha, I. Sarnoff, J. Weston, F. Arneodo, A. Di Giovanni, *et al.*, *Phys. Rev. D* **105**, 052010 (2022).
- [32] A. J. Millar, G. G. Raffelt, J. Redondo, and F. D. Steffen, *J. Cosmol. Astropart. Phys.* **2017** (01), 061.
- [33] D. Horns, J. Jaeckel, A. Lindner, A. Lobanov, J. Redondo, and A. Ringwald, *J. Cosmol. Astropart. Phys.* **2013** (04), 016.
- [34] J. I. Read, *J. Phys. G: Nucl. Part. Phys.* **41**, 063101 (2014).
- [35] S. Ghosh, E. Ruddy, M. Jewell, A. Leder, and R. Maruyama, *Phys. Rev. D* **104**, 092016 (2021).

- [36] M. T. Sebastian, R. Ubic, and H. Jantunen, *International Materials Reviews* **60**, 392 (2015).
- [37] N. M. Alford, J. Breeze, X. Wang, S. J. Penn, S. Dalla, S. J. Webb, N. Ljepojevic, and X. Aupi, *Journal of the European Ceramic Society* **21**, 2605 (2001).
- [38] R. Cervantes, G. Carosi, S. Kimes, C. Hanretty, B. LaRoque, G. Leum, P. Mohapatra, N. Oblath, R. Ottens, Y. Park, *et al.*, *Phys. Rev. D* **106**, 102002 (2022).
- [39] E. Aprile and *et al.*, *Phys. Rev. D* **106**, 022001 (2022).
- [40] P. Arias, D. Cadamuro, M. Goodsell, J. Jaeckel, J. Redondo, and A. Ringwald, *J. Cosmol. Astropart. Phys.* **2012** (06), 013.
- [41] S. Knirck, T. Yamazaki, Y. Okesaku, S. Asai, T. Idehara, and T. Inada, *J. Cosmol. Astropart. Phys.* **2018** (11), 031.
- [42] L. Krauss, J. Moody, F. Wilczek, and D. E. Morris, *Phys. Rev. Lett.* **55**, 1797 (1985).
- [43] M. S. Turner, *Phys. Rev. D* **42**, 3572 (1990).
- [44] B. Brubaker, L. Zhong, S. Lamoreaux, K. Lehnert, and K. van Bibber, *Phys. Rev. D* **96**, 123008 (2017).

### Appendix A: The schematic diagram of the experimental apparatus

The schematic diagram of the experimental apparatus is shown in Fig. 5, and the more details of the receiver chain is given. Amplifier 1 and Amplifier 2 were millimeter-wave low noise amplifiers working at 65 ~ 110 GHz, which provided a total gain of around 60 dB. The input noise of Amplifier 1 was the predominant source of the receiver chain noise. The down-conversion was achieved by two-step frequency mixing. Local oscillator 1 supplied a fixed local oscillating signal of 84.5 GHz. The Filter 1 was introduced to suppress the image-frequency noise of Amplifier 1 during the first frequency mixing. Local oscillator 2 offered a tuning local oscillating signal from 9.2 GHz to 9.9 GHz, which enabled a dark photon searching band of 0.8 GHz. An IQ mixer and 90 degree hybrid coupler were employed to suppress the image-frequency noise during the second mixing. The down-converted signal at baseband frequency (< 205 MHz) was finally acquired by a FPGA-based DAQ board, which was equipped with 1 GHz sampling rate and 250 MHz bandwidth.

### Appendix B: The reflectivity tests

The reflectivity test results of the four LaAlO<sub>3</sub> disks are shown in Fig. 6. Disk 1~4 denote the four disks from bottom to top in the stack. The loss angles  $\delta_{\text{single}}$  obtained from the single disk tests were  $(4.24 \pm 0.43) \times 10^{-2}$ ,  $(3.50 \pm 0.42) \times 10^{-2}$ ,  $(4.01 \pm 0.44) \times 10^{-2}$  and  $(4.49 \pm 0.42) \times 10^{-2}$ , respectively. The results of  $\delta_{\text{single}}$  were different from the stack loss angles  $\delta$ . This is because of the installation difference between single disk

and stack test, which led to varied three-dimensional effects.

We conducted the stack reflectivity test at 2024-12-27 and 2025-02-14, separately. The results demonstrated that the stack remained quite stable within a long period, as shown in Fig. 7. The fitting results on two tests gave a stack amplification parameter relative deviation as  $\sim 0.1\%$ , which was negligible compared with the uncertainty brought by stack parameter uncertainties. The uncertainty of amplification parameter was obtained by Monte Carlo method through randomly scanning the stack parameters within their 95% confidence intervals, as list in the main text.

### Appendix C: Calibration of the antenna receiving efficiency

To characterize the antenna receiving efficiency  $\eta_r$ , the transmission efficiency test of the antenna was implemented. We positioned two same antennas (A and B) face to face with distance  $d = 4.3$  cm, which equaled the distance between stack top and antenna as shown in Fig. 5. The antenna B was the used one in the dark photon search experiment. The measured energy transmission efficiency (S21) from antenna A to antenna B is as shown in Fig. 8. Notably, the energy transmission efficiency was a lower-bound value of antenna B receiving efficiency, since the emission efficiency of antenna A was below one. The minimum value of S21 from 93.750 GHz to 94.550 GHz was taken as a conservative value of antenna B receiving efficiency  $\eta_r$ , which was 0.48.

### Appendix D: Characterization of the receiver chain

In this work, we conducted the dark photon search at eight overlapped frequency ranges (frequency range 1~8, see more details in section E), by changing the local oscillator 2 frequency from 9.2 GHz to 9.9 GHz (corresponding to total local oscillator frequency from 93.7 GHz to 94.4 GHz), with a step of 100 MHz. The characterization of receiver chain was also implemented at those eight frequency ranges, independently.

To map the output of DAQ board to the input power of receiver chain, the coefficient  $\beta$  was calibrated first. By inputting a calibration signal with known power at the input of Amplifier 2, we measured the DAQ output at different frequencies. The gain of Amplifier 1 and insertion loss of waveguide as well as Filter 1 were calibrated accurately with millimeter-wave vector network analyzer, resulting in an effective gain of  $33.9 \pm 0.4$  dB from 93.750 GHz to 94.550 GHz. Then, the coefficient  $\beta$  was given by the results above. The coefficient result in the frequency range of 94.014 GHz ~ 94.202 GHz (frequency range 4) is shown in Fig. 9,

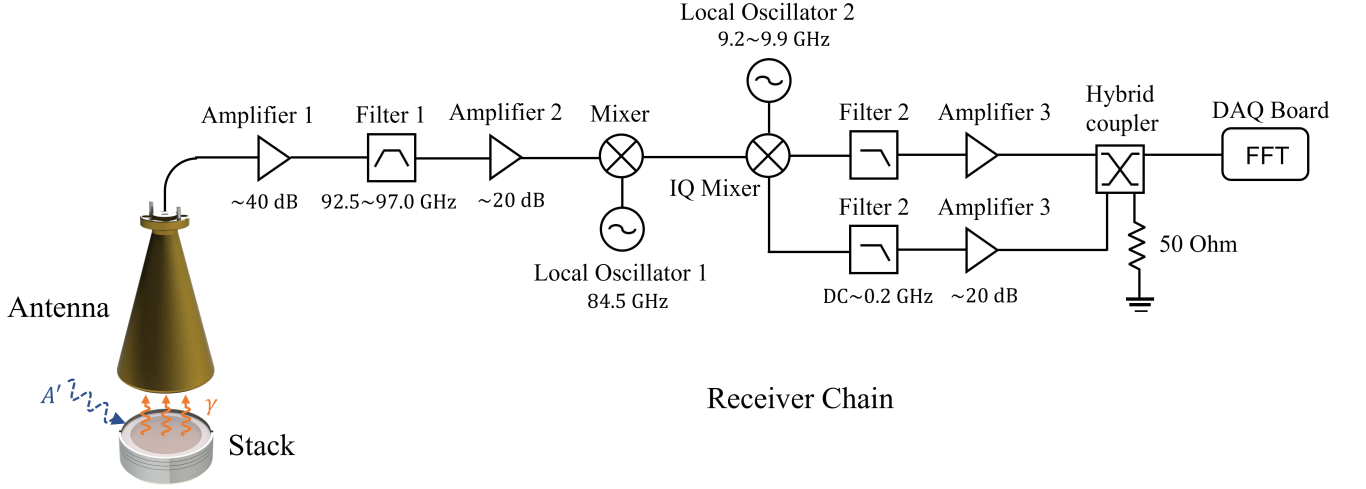


FIG. 5. Schematic diagram of the experiment apparatus for dark photon search.

the shaded region denotes the uncertainty ( $\pm 1\sigma$ ) of  $\beta$ . The uncertainty of  $\beta$  consists of the uncertainties of calibration signal power, effective gain and DAQ output value. During the DAQ output measurement, the local oscillator frequency  $f_{LO}$  was calibrated at the same time. The calibration signal and DAQ board was triggered by one atomic clock, and  $f_{LO}$  was given by the difference between signal frequency and baseband frequency. Frequency stability test of the receiver chain was implemented by monitoring the baseband frequency on DAQ board, with fixed calibration signal and local oscillator frequency. Within a 24 hours monitoring, the variation range of the baseband frequency was 22.8 kHz. The fluctuation of receiver chain frequency would cause attenuation of a expected dark photon signal. By simulation on a hypothetical dark photon signal, the attenuation was 1.00 (0.97 ~ 1.00), the first quartile 0.97 was selected as a conservative estimation of the attenuation factor  $\eta_f$ .

## Appendix E: Details of data analysis

### 1. Candidate peaks analysis

We conducted the dark photon search at eight overlapped frequency ranges, and the data acquisition time was about 24 hours at each frequency range. After the averaging and baseline-removal procedure (see more details in Subsection E 2), a total of twenty candidate peaks (Peak 1 to Peak 20) at different frequencies were discovered within the eight frequency ranges, as shown in Fig. 10. Sixteen of the candidate peaks (Peak 1~11, 13, 14, 17~19) were not found in the result of neighboring frequency range, thus they were identified as spurious signals and ruled out. The rest four candidates (Peak 12,

15, 16, 20) were subjected to further analysis and found to have a similar linewidth around 12 kHz. Since the linewidth was far from the expected dark photon signal  $\Delta f_{A'} \approx 94$  kHz, these four candidate peaks were also rejected.

Besides the peaks mentioned above, there were seven deeps in the results of frequency range 2~8. The deeps all had a similar linewidth around 200 kHz, and all occurred at the same baseband frequency around 18 MHz. Those deeps, also spurious signals, were induced by the DAQ board or Amplifier 3.

### 2. Details of data analysis procedures

In this subsection, some details of the data analysis procedures are provided. During the data collection time of eight days, a total of  $5 \times 10^8$  spectra were acquired, and at each frequency range the number was around  $6 \times 10^7$ . The acquired spectra were averaged by 5100 times on DAQ board, before saved. The frequency bin width  $\delta f$  of each spectrum was set as 7.63 kHz. Here we took the data of 94.014 GHz ~ 94.202 GHz (frequency range 4) as example. The saved 124010 spectra were averaged to a signal raw spectrum  $P'_{\text{raw}}$ . The raw spectrum  $P'_{\text{raw}}$  was multiplied by coefficient  $\beta$  to obtain the raw power spectrum  $P_{\text{raw}}$ , which is shown in Fig. 11(a). Firstly, the raw power spectrum  $P_{\text{raw}}$  was filtered by a 4th-order Savitzky-Golay (SG) filter with a window length of 1.14 MHz [38]. Notably, the SG filter would attenuate a potential dark photon signal by  $\eta_{\text{SG}} = 0.74$ . The value of  $\eta_{\text{SG}}$  was obtained by comparing the simulated dark photon signal amplitude before and after the SG filtering. The filtered baseline is shown as the red line in Fig. 11(a), which was the average noise power  $P_n$  of the receiver chain during the data acquisition. The receiver

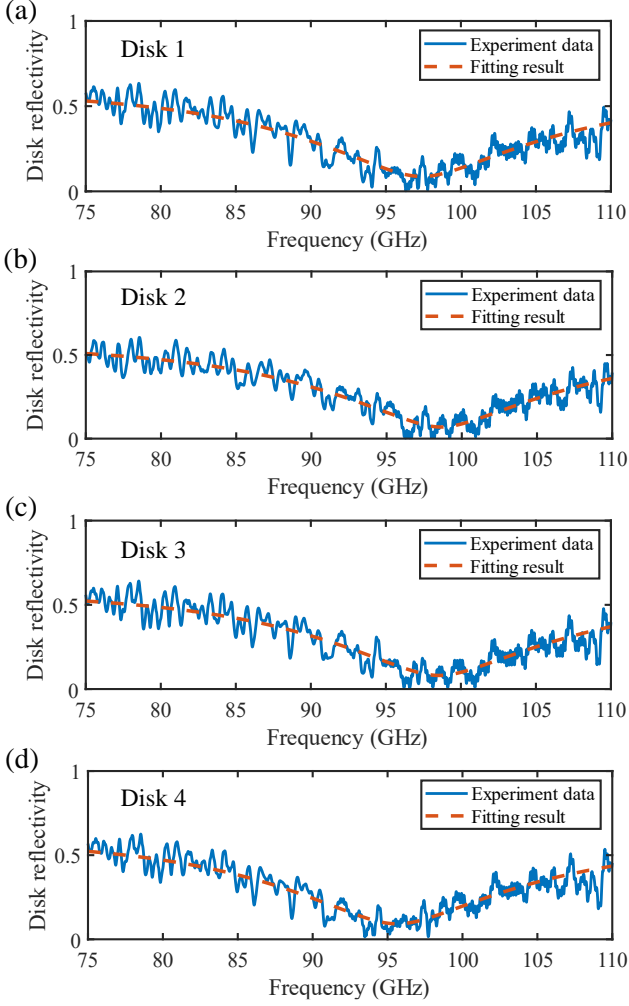


FIG. 6. The reflectivity tests of the rest dielectric disks. (a)~(d) The reflectivity and fitting results of Disk 1~4.

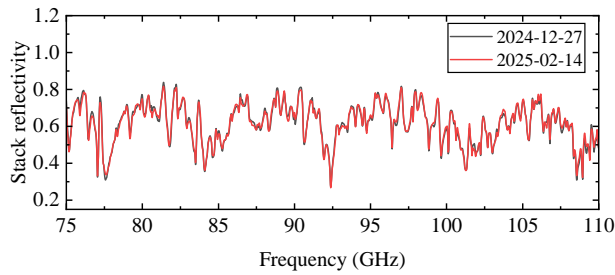


FIG. 7. The reflectivity tests of the stack at 2024-12-27 and 2025-02-14, respectively.

chain noise fluctuated slightly ( $\sim 1\%$ ) during the data acquisition time, which was considered as the system uncertainty of  $P_n$ . Then we obtained the raw power excess  $\Delta_{\text{raw}}$  as

$$\Delta_{\text{raw}} = \frac{P_{\text{raw}}}{P_n} - 1, \quad (\text{E1})$$

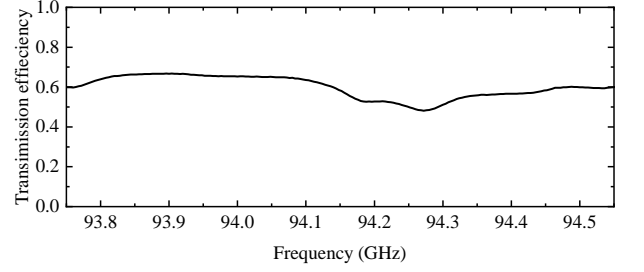


FIG. 8. The result of antenna transmission efficiency.

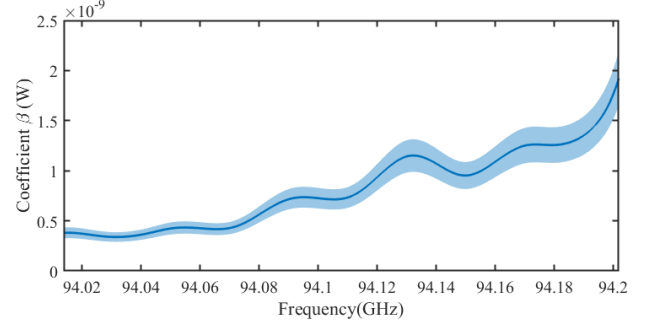


FIG. 9. The calibrated coefficient  $\beta$  of frequency range 4, which is from 94.014 GHz to 94.202 GHz. The shaded region denotes the  $\pm 1\sigma$  uncertainty of  $\beta$ .

The raw power excess  $\Delta_{\text{raw}}$  before discarding the spurious signals is shown in Fig. 11(b), the two spurious signals in this frequency range are shown in Fig. 11(c) and Fig. 11(d), respectively. Then the bins occupied by spurious signals were discarded from the raw power excess. The normalized raw power excess  $\Delta_{\text{norm,raw}}$  was obtained by dividing the standard deviation  $\sigma_{\text{raw}}$  of raw power excess. As shown in Fig. 12(a), there are no bins exceeding  $5\sigma_{\text{raw}}$  in  $\Delta_{\text{norm,raw}}$  after discarding the spurious signals. The distribution of normalized raw power excess  $\Delta_{\text{norm,raw}}$  fitted well with the unit Gaussian distribution, with mean  $\mu = -4.4 \times 10^{-5} \pm 0.12$  and standard deviation  $\sigma = 1.0 \pm 0.0089$  obtained from fitting result, as illustrated by the red line in Fig. 12(b). The raw power excess was multiplied by noise power  $P_n$  to be related to real power. Then the raw power excess was rescaled to the dark photon signal with  $\chi = 1$ , as shown in Fig. 13(a). The rescaled power excess  $\Delta_r$  is represented as

$$\Delta_r = \Delta_{\text{raw}} \frac{P_n}{\eta_r P_s(\chi = 1)}, \quad (\text{E2})$$

where  $\eta_r$  is the antenna receiving efficiency.  $P_s(\chi)$  is the expected dark photon signal induced by stack with a specific  $\chi$ , and the attenuation factor  $\eta_{\text{SG}}$  and  $\eta_f$  were considered when calculating  $P_s(\chi = 1)$ . To enhance the SNR, the rescaled power excess  $\Delta_r$  was convolved with the dark photon line shape, which can be described by



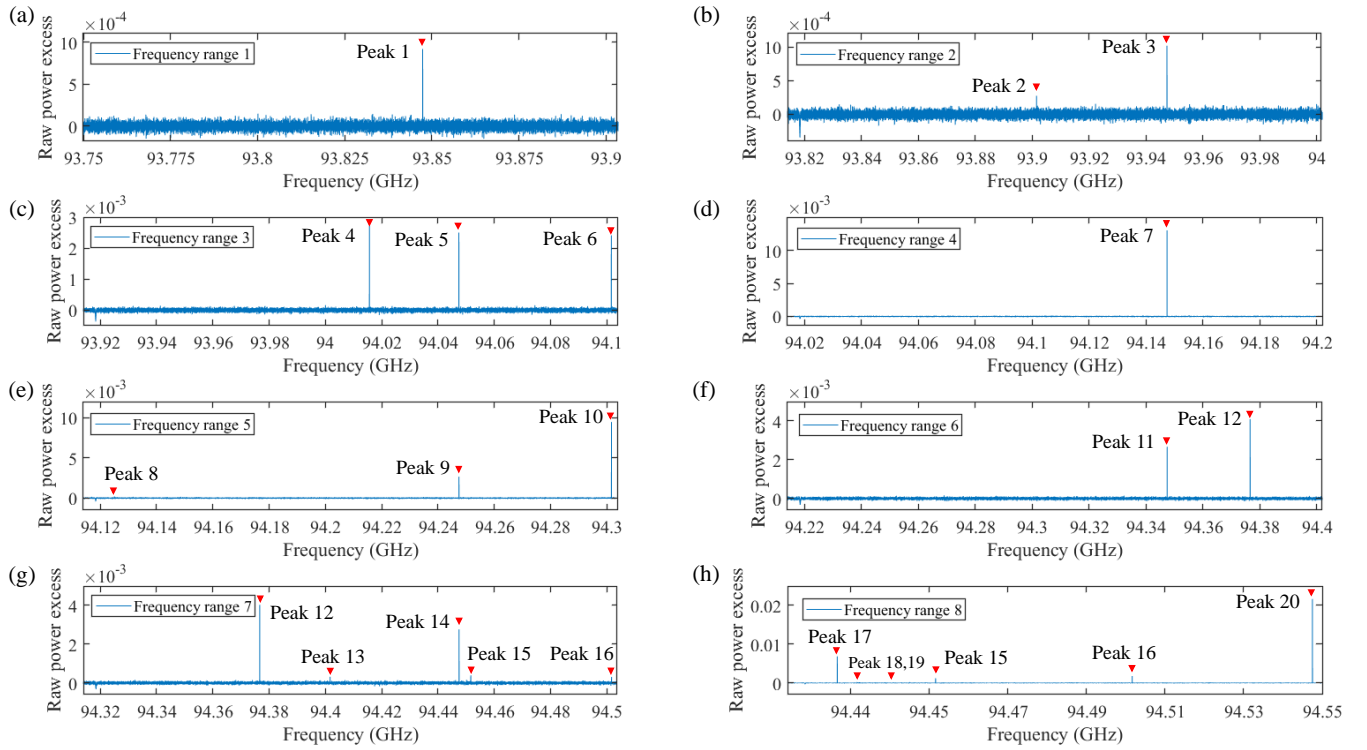


FIG. 10. The raw power excess results  $\Delta_{\text{raw}}$  of eight frequency ranges, which are obtained after the averaging and baseline-removal procedure of raw spectra. There are twenty suspicious peaks within the eight frequency ranges. Peak 1~11, 13, 14, 17~19 do not exist in the result of neighboring frequency range. Peak 12, 15, 16, 20 are found to have insufficient linewidth to be dark photon signals.

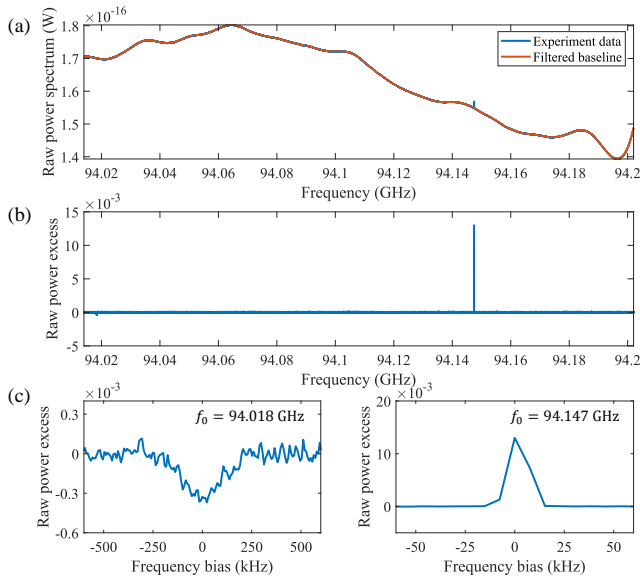


FIG. 11. (a) The raw power spectrum  $P_{\text{raw}}$  and the SG filter result. (b) The raw power excess  $\Delta_{\text{raw}}$  after the baseline removal operation, before discarding the spurious signals. (c)~(d) Zoomed-in view of two spurious signals in frequency range 4.

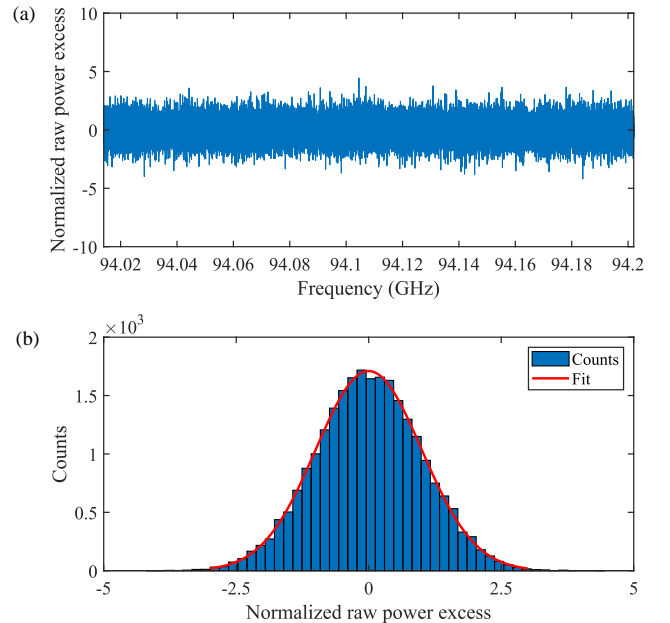


FIG. 12. (a) The normalized raw power excess  $\Delta_{\text{norm,raw}}$ . (b) The distribution of normalized raw power excess and fitting result with unit Gaussian distribution.

the Maxwell-Boltzmann distribution:

$$\mathcal{F} = 2\sqrt{\frac{f-f_a}{\pi}} \left[ \frac{3}{\eta_c f_a \langle (v_a/c)^2 \rangle} \right]^{3/2} \exp\left(\frac{-3(f-f_a)}{\eta_c f_a \langle (v_a/c)^2 \rangle}\right), \quad (\text{E3})$$

where  $f_a$  is the frequency of dark photon,  $c$  is the velocity

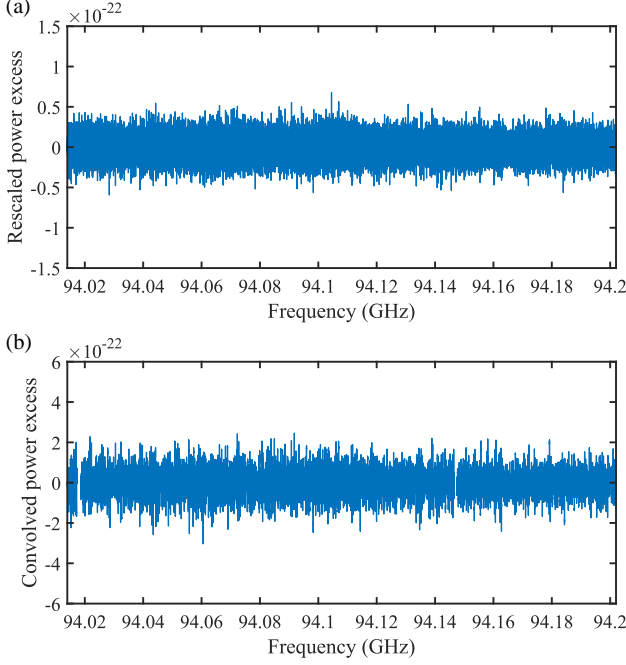


FIG. 13. (a) The rescaled power excess  $\Delta_r$ . (b) The convolved power excess  $\Delta$ . Since the window length of convolution was 100 bins, extral 100 bins near spurious signals were discarded during the convolution.

of light,  $v_a$  is the velocity of dark photon, and  $\eta_c$  is a correction factor introduced by the complex motion of the lab frame. Here  $\langle v_a^2 \rangle = (270 \text{ km/s})^2$  and  $\eta_c = 1.7$  was adopted [42–44]. The convolution window was set as 763 kHz or 100 bins. Then we finally obtained the convolved power excess  $\Delta$ , as shown in Fig. 13(b). The corresponding normalized power excess  $\Delta_{\text{norm}} = \Delta/\sigma$  is shown in Fig 14, where  $\sigma$  is the standard deviation of convolved power excess  $\Delta$ . A hypothetical dark photon signal with  $\chi = 2.5 \times 10^{-11}$  at 94.100 GHz is shown in the inset of Fig. 14. The hypothetical dark photon signal was obvious and exceeded  $5\sigma$ .

The systematic uncertainties are listed in Table I, and the total systematic uncertainty  $\sigma_{\text{sys}}$  was obtained by adding the individual uncertainties in quadrature. Then the total uncertainties  $\sigma'$  were given by

$$\sigma' = \sqrt{\sigma^2 + \Delta^2 \sigma_{\text{sys}}^2}, \quad (\text{E4})$$

where  $\Delta$  is the convolved power excess,  $\sigma$  is the standard deviation or statistic uncertainty of  $\Delta$ . The total uncertainties  $\sigma'$  were utilized to set constraints on kinetic mixing  $\chi$ .

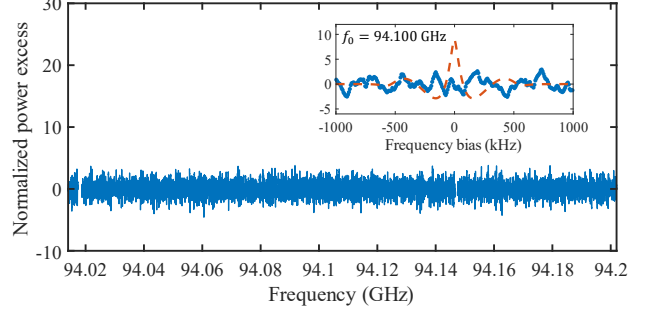


FIG. 14. The normalized power excess  $\Delta_{\text{norm}}$  of frequency range 4. The inset shows a hypothetical dark photon signal with  $\chi = 2.5 \times 10^{-11}$  at 94.100 GHz (red dashed line), compared with the observation data (blue dots).

In this work, Bayesian analysis was employed to provide constraints of the kinetic mixing  $\chi$  [38]. For a given dark photon signal  $P_s$ , the measured power excess  $\Delta_m$  followed the distribution as

$$p(\Delta_m | P_s) = \frac{1}{\sqrt{2\pi}\sigma_m} \exp\left[-\frac{(\Delta_m - P_s)^2}{2\sigma_m^2}\right], \quad (\text{E5})$$

where  $\sigma_m$  is the uncertainty of measured power excess  $\Delta_m$ . Since the dark photon signal  $P_s$  was in the unit of  $P_s(\chi = 1)$ , it could be replaced by  $\chi^2$ :

$$p(\Delta_m | \chi^2) = \frac{1}{\sqrt{2\pi}\sigma_m} \exp\left[-\frac{(\Delta_m - \chi^2)^2}{2\sigma_m^2}\right], \quad (\text{E6})$$

By employing the Bayesian analysis theory, the distribution of  $\chi^2$  could be represented as [27]

$$p(\chi^2 | \Delta) = \frac{p(\Delta | \chi^2)}{\int_0^{+\infty} p(\Delta | \chi^2) d\chi^2}, \quad (\text{E7})$$

where  $\Delta_m$  and  $\sigma_m$  are replaced by experiment results  $\Delta$  and  $\sigma'$ . Finally, by solving the equation

$$\int_0^{\chi_{90\%}^2} p(\chi^2 | \Delta) d\chi^2 = 90\%, \quad (\text{E8})$$

for each bin, the constraints on kinetic mixing  $\chi$  with a confidence level of 90% were obtained. Constraint results of eight frequency ranges were combined by selecting the lower constraint at every overlapped frequency bin. The combined constraints are shown in Fig.4 of the main text, there are four gaps at 94.377 GHz, 94.452 GHz, 94.502 GHz and 94.548 GHz, which are caused by Peak 12, 15, 16 and 20, respectively.

TABLE I. Summary of the relative systematic uncertainties of experiment parameters. The first and second values (if necessary) denote the minimum and maximum uncertainties within the frequency range from 93.750 GHz to 94.550 GHz.

Parameter	Relative uncertainty
Coefficient $\beta$	12.1%
Noise of receiver chain $P_n$	0.7% $\sim$ 5.9%
Area of Disk $A^a$	1.2%
Stack amplification parameter $ \mathcal{B} ^2$	16.6% $\sim$ 20.1%

<sup>a</sup> Note a.  $A = \frac{\pi D^2}{4}$ , where  $D$  is the inner diameter of aluminum holder.